ChemPubSoc Europe

DOI: 10.1002/open.201900219

Open Access ChemistryOPEN Full Papers

Influence of Adding Molybdenum on Structure and Performance of Fe_xO_y/SBA-15 Catalysts in Selective Oxidation of Propene

Nina Sharmen Genz and Thorsten Ressler*[a]

Mixed iron and molybdenum oxide catalysts supported on nanostructured silica, SBA-15, were synthesized with various Mo/Fe atomic ratios ranging from 0.07/1.0 to 0.57/1.0. Structural characterization of as-prepared Mo_xO_y_Fe_xO_y/SBA-15 samples was performed by nitrogen physisorption, X-ray diffraction, and DR-UV-Vis spectroscopy. Adding molybdenum resulted in a pronounced dispersion effect on supported iron oxidic species. Increasing atomic ratio up to 0.21Mo/1.0Fe was accompanied by decreasing species sizes. Strong interactions between iron and molybdenum during the synthesis resulted in the formation of Fe–O–Mo structure units, possibly $Fe_2(MoO_4)_3$-like species. Reducibility of Mo_xO_y_Fe_xO_y/SBA-15 catalysts was investigated by temperature-programmed reduction experiments with hydrogen as reducing agent. The lower reducibility obtained when adding molybdenum was ascribed to both dispersion and electronic effect of molybdenum. Catalytic performance of Mo_xO_y_Fe_xO_y/SBA-15 samples was studied in selective gas-phase oxidation of propene with O_2 as oxidant. Adding molybdenum resulted in an increased acrolein selectivity and a decreased selectivity towards total oxidation products.

1. Introduction

The awareness for the depleting of our fossil feedstocks resources has been growing in the last years. The search for alternatives to fossil feedstocks, like, for example, bio-based feedstocks, is ongoing.[1–3] Green chemistry aims to achieve the overall goal of sustainability for chemical processes. Chemical processes conform with green chemistry if they are less toxic for human health and environment.[4] This affects also the selective oxidation of propene. Propene is the second most demanded product in petrochemical industry.[5] Glycerol as possible new bio-based feedstock for synthesis of acrolein recently attracted attention in catalysis research. Glycerol is abundantly available and relatively inexpensive as a by-product from biodiesel production. It can be transformed to acrolein by catalytic dehydration.[2,3] However, this bio-based synthesis route is still in its early stages and considerable research effort is required for generating an industrially applicable process. Therefore, interest in further improvement of already well-investigated selective oxidation of propene to acrolein reappeared. An improvement in both selectivity towards acrolein and propene conversion would lead to a considerably increased cost efficiency. Moreover, selective oxidation of propene would become greener. Such an improvement might be realized by optimized or newly designed catalysts. However, catalysts applied in selective oxidation reactions are highly complex and seem to become more complex with increasing efficiency. Rational catalyst design constitutes a promising alternative to conventional trial-and-error approach in developing optimized catalysts.[6,7] Rational catalyst design requires an in-depth understanding of reliable structure-activity correlations.

Revealing reliable structure-activity correlations requires reducing chemical and structural complexity of industrial applied catalysts to model catalysts. In heterogeneous catalysis, catalytic reactions occur on the surface of the catalysts, while the surface structure differs significantly from that of the bulk. Therefore, dispersing metal oxides on well-defined support materials may result in suitable model catalysts. For elucidating structure-activity correlations, a detailed knowledge of structure, composition, and certain chemical functions of the model catalysts is indispensable. Thus, determining the important variables for structure and catalytic performance of model catalysts is a starting point for a rational design of improved catalysts.

In terms of green chemistry, the search for alternative greener catalysts becomes more relevant. Iron is the second most abundant metal and constitutes 4.7 wt% of the earth crust.[8] Therefore, iron-based catalysts constitute a promising alternative to more expensive metal catalysts. Moreover, various iron compounds are commercially available or easy to synthesize. The probably most important advantage in view of principles of green chemistry, is that iron is less toxic for human health and environment.[4,9] Furthermore, Fe^{2+}/Fe^{3+} are often used as redox promotors to improve redox properties of selective oxidation catalysts.[7,10,11] Replacing less environmentally friendly and more expensive metals by iron without diminishing catalytic performance would be an advancement in catalysis research.

[a] N. S. Genz, Prof. Dr. T. Ressler
Institut für Chemie
Technische Universität Berlin
Straße des 17. Juni 135
10623 Berlin, Germany
E-mail: thorsten.ressler@tu-berlin.de

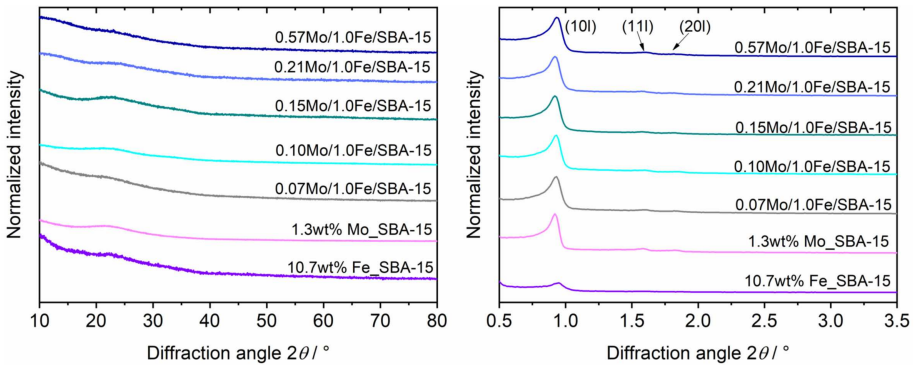

Figure 1. Left: Wide-angle X-ray diffraction patterns of Mo_xO_y_Fe_xO_y/SBA-15 samples at various Mo/Fe atomic ratios, 1.3 wt% Mo_SBA-15, and 10.7 wt% Fe_SBA-15. Right: Small-angle X-ray diffraction patterns of Mo_xO_y_Fe_xO_y/SBA-15 samples, 1.3 wt% Mo_SBA-15, and 10.7 wt% Fe_SBA-15.

Currently, catalysts employed for the industrial synthesis of acrolein are complex multicomponent metal oxides. Examples for applied metals are bismuth, molybdenum, iron, vanadium, cobalt, nickel, and tungsten.[12] In this work, a binary model catalyst system was synthesized by changing the chemical composition of the green Fe_xO_y/SBA-15 catalysts by adding molybdenum. Therefore, iron and molybdenum mixed oxides supported on SBA-15 were synthesized and characterized regarding structure, reducibility, and catalytic performance in selective oxidation of propene. An interpretation of molybdenum induced differences in structure and reducibility of Fe_xO_y/SBA-15 and their influence on catalytic performance was eventually presented.

2. Results and Discussion

2.1. Structural Characterization of Mo_xO_y_Fe_xO_y/SBA-15 Catalysts

2.1.1. Mesoporous Structure of Mo_xO_y_Fe_xO_y/SBA-15

2.1.1.1. Long-Range Ordered Structure

Long-range ordered structure of the Mo_xO_y_Fe_xO_y/SBA-15 samples was investigated by wide-angle and small-angle X-ray diffraction. Figure 1, left depicts wide-angle X-ray diffraction patterns of all Mo_xO_y_Fe_xO_y/SBA-15 samples, 1.3 wt% Mo_SBA-15, and 10.7 wt% Fe_SBA-15. The absence of sharp diffraction peaks was indicative of no long-range ordered phases and high dispersion of small iron and molybdenum oxides within the Mo_xO_y_Fe_xO_y/SBA-15 samples. Additionally, neither Mo_xO_y nor Fe_xO_y species of the reference samples showed a long-range ordering. The broad diffraction peak at 23° 2θ corresponded to the amorphous SBA-15 support material.[13] Small-angle diffraction patterns of all samples exhibited characteristic diffraction peaks (10 l), (11 l), and (20 l) of SBA-15 (Figure 1, right).[14,15] Hence, two-dimensional hexagonal symmetry of the support material SBA-15 was retained after supporting iron and molybdenum oxides.

2.1.1.2. Surface and Porosity Characteristics

N_2 physisorption measurements were conducted for determining specific surface area and investigating pore structure of the Mo_xO_y_Fe_xO_y/SBA-15 samples, 1.3 wt% Mo_SBA-15, and 10.7 wt % Fe_SBA-15. All samples exhibited type IV nitrogen adsorption/desorption isotherms with H1 hysteresis loops indicating mesoporous materials (Figure 2).[16] Adsorption and desorption branches were nearly parallel at the hysteresis loop, as expected for regularly shaped pores. However, a knee in the hysteresis loop was observed for all Mo_xO_y_Fe_xO_y/SBA-15 samples except for sample 1.3 wt% Mo_SBA-15. A knee in the hysteresis loop might have three possible reasons. First, synthesis procedure could have varied the structure of SBA-15. A changed SBA-15 structure was excluded based on XRD results confirming structure preservation. Furthermore, despite the observed knee in the hysteresis loop, N_2 adsorption/desorption isotherms of all samples were identified to be type IV with H1 hysteresis loop, being characteristic for SBA-15 support material. Second, partially blocked mesopores of SBA-15 could have yielded a knee in the hysteresis loop. This possible reason was also excluded since desorption and adsorption branches converged

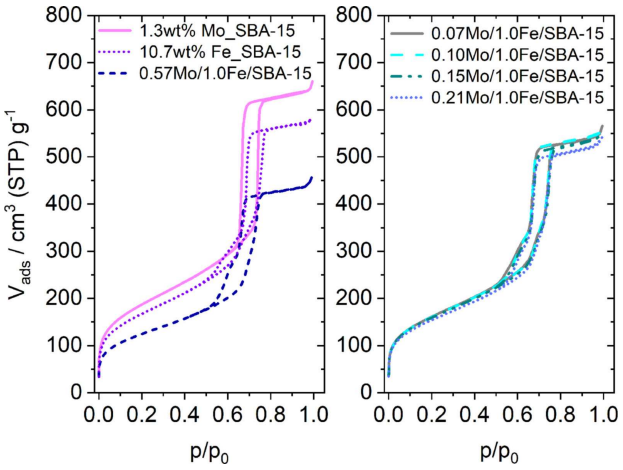

Figure 2. N_2 adsorption/desorption isotherms of Mo_xO_y_Fe_xO_y/SBA-15 samples, 1.3 wt% Mo_SBA-15, and 10.7 wt% Fe_SBA-15.

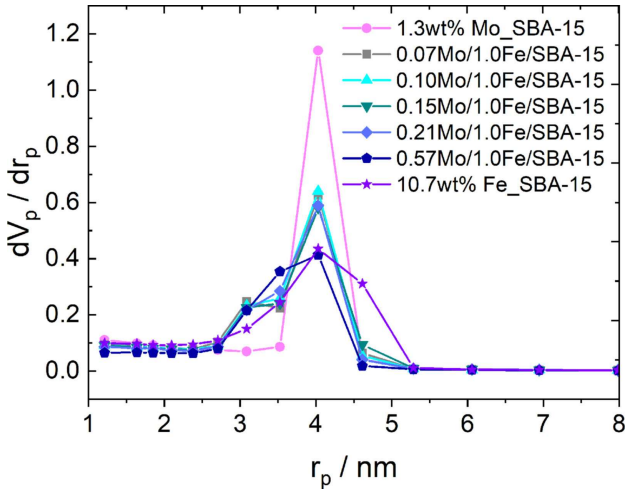

Figure 3. Pore radius distribution of Mo_xO_y_Fe_xO_y/SBA-15 samples, 1.3 wt% Mo_SBA-15, and 10.7 wt% Fe_SBA-15.

after the hysteresis loop at higher p/p_0, and all samples possessed similar pore radius distributions (Figure 3). Besides, partial blocking of mesopores, as reported for CuNi/SBA-15 (5 wt% Cu, 5 wt% Ni),[17] NiO/SBA-15 (24 wt% Ni),[18] or CoMoW/SBA-15 (9 wt% MoO_3, 14 wt% WO_3, 4 wt% CoO),[19] was always associated with pronounced two-step desorption branches, whereas adsorption branches were unaffected. Hence, the third possible reason, a bimodal particle size distribution, seemed to be reasonable. The knee in the hysteresis loop of the Mo_xO_y_Fe_xO_y/SBA-15 samples, was probably induced by bimodal particle size distributions, complying with pore radius distributions determined by BJH method. Samples 0.07Mo/1.0Fe/SBA-15, 0.10Mo/1.0Fe/SBA-15, 0.15Mo/1.0Fe/SBA-15, and 0.21Mo/1.0Fe/SBA-15 showed a bimodal pore radius distribution with a main maximum at 4.0 nm and a second maximum at ~3–3.5 nm. In contrast, pore radius distribution of 1.3 wt% Mo_SBA-15 was narrow with a sharp maximum at 4.0 nm and that of 0.57Mo/1.0Fe/SBA-15 was broad and ranged from ~2.6 through ~4.6 nm (Figure 3). Pore radius distribution of 10.7 wt% Fe_SBA-15 showed a main maximum at 4.0 nm. Differences in pore radius contributions dependent on Mo/Fe atomic ratio probably originated from various interactions between molybdenum and iron during synthesis. At low Mo/Fe atomic ratios, significantly higher amounts of iron compared to molybdenum were present in the Mo_xO_y_Fe_xO_y/SBA-15 samples. Hence, only a small fraction of iron atoms directly interacted with molybdenum atoms during synthesis, resulting in a bimodal particle size distribution. Fe_xO_y species which were directly influenced by molybdenum atoms differed in species size compared to Fe_xO_y without direct influence of molybdenum atoms. Accordingly, differences in chemical environment during synthesis were probably responsible for bimodal particle size distributions, and hence, for the knee in the hysteresis loop of N_2 adsorption/desorption isotherms of the Mo_xO_y_Fe_xO_y/SBA-15 samples. For sample 0.57Mo/1.0Fe/SBA-15, possessing a more balanced Mo/Fe atomic ratio, such differences in chemical environment were less pronounced. The higher Mo/Fe atomic ratio effected more balanced interactions between iron and molybdenum atoms during synthesis, inducing a broadened particle size distribution. However, the broadened particle size distribution agreed with the knee in the hysteresis loop because of the excess of iron compared to molybdenum.

The specific surface area, $a_{s,BET}$, of Mo_xO_y_Fe_xO_y/SBA-15 samples systematically decreased with increasing Mo/Fe atomic ratio. Whereas SBA-15 possessed a specific surface area between 706.8 and 756.8 m^2/g, surface areas determined after supporting iron and molybdenum oxides were between 447.6 and 675.7 m^2/g. This decrease in $a_{s,BET}$ together with a decrease in pore volume, V_{pore}, from 1.036–1.203 cm^3/g of SBA-15 to 0.705–1.012 cm^3/g of as-prepared samples, indicated the iron and molybdenum species being successfully located in the mesopores of SBA-15. Details on surface and porosity characteristics evaluated by N_2 physisorption and XRD measurements are summarized in Table 1.

Mesopore surface area, a_{pore}, calculated by BJH method[20] and specific surface area, $a_{s,BET}$, calculated by BET method[21] can be used for estimating the contribution of micropores to the entire surface area of SBA-15.[22,23] Therefore, the ratio of mesopore surface area and specific surface area, $a_{pore}/a_{s,BET}$, was calculated (Table 1). For Mo_xO_y_Fe_xO_y/SBA-15 samples with atomic ratios between 0.07Mo/1.0Fe and 0.21Mo/1.0Fe, ratio of $a_{pore}/a_{s,BET}$ was nearly invariant at 0.91 and 0.90, respectively. Ratio of $a_{pore}/a_{s,BET}$ of 0.91 was also obtained for sample 10.7 wt % Fe_SBA-15, the Fe_xO_y/SBA-15 sample without molybdenum

Table 1. Surface and porosity characteristics of Mo_xO_y_Fe_xO_y/SBA-15 samples, sample 1.3 wt% Mo_SBA-15, and sample 10.7 wt% Fe_SBA-15. [a]

	$a_{s,BET}/m^2/g$[b]	$V_{pore}/cm^3/g$[c]	$a_{pore}/a_{s,BET}$[d]	a_0/nm[e]	d_w/nm[f]	ΔD_f[g]
1.3 wt% Mo_SBA-15	675.7 ± 0.7	1.012 ± 0.001	0.88	11.14 ± 0.01	3.08 ± 0.01	0.06 ± 0.02
0.07Mo/1.0Fe/SBA-15	581.1 ± 0.6	0.865 ± 0.001	0.91	11.09 ± 0.01	3.03 ± 0.01	0.11 ± 0.02
0.10Mo/1.0Fe/SBA-15	579.1 ± 0.6	0.869 ± 0.001	0.91	11.01 ± 0.01	2.95 ± 0.01	0.13 ± 0.01
0.15Mo/1.0Fe/SBA-15	573.2 ± 0.6	0.851 ± 0.001	0.90	11.17 ± 0.01	3.11 ± 0.01	0.11 ± 0.02
0.21Mo/1.0Fe/SBA-15	554.7 ± 0.7	0.832 ± 0.001	0.91	11.18 ± 0.01	3.12 ± 0.01	0.14 ± 0.02
0.57Mo/1.0Fe/SBA-15	447.6 ± 0.4	0.705 ± 0.001	0.96	11.05 ± 0.01	2.99 ± 0.01	0.27 ± 0.03
10.7 wt% Fe_SBA-15	605.7 ± 0.6	0.898 ± 0.001	0.91	10.94 ± 0.01	2.88 ± 0.01	0.15 ± 0.02

[a] Measurement errors according to standard deviation determined from multiple measurements. [b] Specific surface area, $a_{s,BET}$, was calculated in the relative pressure range, p/p_0, of 0.05–0.25. [c] Pore volume, V_{pore}, is based on relative pressure, p/p_0, of 0.99. [d] Ratio of mesopore surface area, a_{pore}, and specific surface area, $a_{s,BET}$, as measure of micropore contribution to the entire surface of SBA-15. [e] Lattice constant, a_0, of hexagonal unit cell. [f] Wall thickness between the mesopores of SBA-15, d_w. [g] Differences in fractal dimension, ΔD_f, between SBA-15 and corresponding Mo_xO_y_Fe_xO_y/SBA-15 samples as measure of the roughness of the surface.

addition. Hence, adding molybdenum at atomic ratios between 0.07Mo/1.0Fe and 0.21Mo/1.0Fe did not affect the contribution of micropores to the entire surface area of SBA-15. A higher atomic ratio of 0.57Mo/1.0Fe induced an increased ratio of $a_{pore}/a_{s,BET}$ up to 0.96 indicating a decreased contribution of micropores. Conversely, an increased contribution of micropores to the entire surface area of SBA-15 was observed for sample 1.3 wt% Mo_SBA-15 possessing a ratio of $a_{pore}/a_{s,BET}$ of 0.88. The low molybdenum loading of this sample correlated with small and highly dispersed molybdenum species. Therefore, a lower degree of micropore filling was observed.

In addition to BET and BJH method, modified FHH method was used to analyze the nitrogen physisorption data. Herein, the fractal dimension D_f was determined as a measure of the roughness of the surface.[22,24] For Mo_xO_y_Fe_xO_y/SBA-15 samples, 1.3 wt% Mo_SBA-15, 10.7 wt% Fe_SBA-15, and SBA-15, the fractal dimension ranged between 2 and 3, indicating a rough surface.[25] In order to elucidate the effect of supported iron and molybdenum species on surface roughness of the support material, ΔD_f values were calculated as difference between D_f values of SBA-15 and those of corresponding Mo_xO_y_Fe_xO_y/SBA-15 samples. For Mo_xO_y_Fe_xO_y/SBA-15 samples with atomic ratios between 0.07Mo/1.0Fe and 0.21Mo/1.0Fe, ΔD_f values were invariant within the error limits. Consequently, adding molybdenum at low Mo/Fe atomic ratios did not influence the surface roughness of SBA-15. An invariant surface roughness of support material at atomic ratios between 0.07Mo/1.0Fe and 0.21Mo/Fe coincided with a nearly invariant contribution of micropores to the entire surface area of SBA-15, $a_{pore}/a_{s,BET}$.

Only for samples 1.3 wt% Mo_SBA-15 and 0.57Mo/1.0Fe/SBA-15, ΔD_f was significantly lower or higher, respectively. For sample 1.3 wt% Mo_SBA-15, consisting of small and highly dispersed Mo_xO_y species, lowest value of ΔD_f agreed with the highest contribution of micropores to the entire surface area of SBA-15. At this low metal oxide loading, most of the pores of SBA-15 remained unfilled, and hence, surface roughness of SBA-15 was only slightly affected. The higher ΔD_f value for sample 0.57Mo/1.0Fe/SBA-15 indicated a smoother surface of SBA-15. The decreased contribution of micropores to the entire surface area of SBA-15 for this sample was in accordance with the smoother surface. Depositing iron and molybdenum oxides in the pores of SBA-15 at higher Mo/Fe atomic ratio resulted in an enhanced micropore filling, accompanied by an enhanced smoothing of the support surface.

2.1.2. Dispersion Effect of Molybdenum on the Size of the Fe_xO_y Species

Figure 4 depicts DR-UV-Vis spectra of all Mo_xO_y_Fe_xO_y/SBA-15 samples, 1.3wt%Mo_SBA-15, and 10.7 wt% Fe_SBA-15. DR-UV-Vis spectra of Mo_xO_y_Fe_xO_y/SBA-15 samples and 10.7 wt% Fe_SBA-15 showed a broad absorption, resulting from overlapping absorption bands, while absorption of sample 1.3 wt% Mo_SBA-15 was significantly narrower.

The average metal oxide particle size was estimated by analyzing the DR-UV-Vis edge energy, determined from the

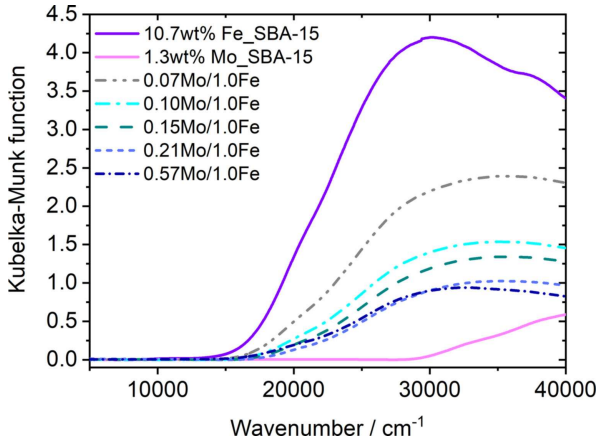

Figure 4. DR-UV-Vis spectra of Mo_xO_y_Fe_xO_y/SBA-15 samples at Mo/Fe atomic ratios between 0.07/1.0 and 0.57/1.0, 1.3 wt% Mo_SBA-15, and 10.7 wt% Fe_SBA-15.

position of the low-energy rise in DR-UV-Vis spectra. Analogous to the model of the particle in the box, decreasing DR-UV-Vis edge energy is reported to correlate with an increasing size of transition metal oxide domain.[13,26,27] DR-UV-Vis edge energies of Mo_xO_y_Fe_xO_y/SBA-15 samples, 1.3 wt% Mo_SBA-15, and iron oxide references were determined according to Weber,[27] and depicted as function of Mo/Fe atomic ratio (Figure 5). Sample 1.3 wt% Mo_SBA-15 possessed the highest value of DR-UV-Vis edge energy, and hence, the smallest Mo_xO_y species size. Determined edge energy of 4.24 eV was close to that reported for mononuclear molybdate species, $[MoO_4]^{2-}$, indicating that this sample mainly consisted of isolated mononuclear Mo_xO_y species.[27,28] The smallest species size together with the presence of mainly isolated, mononuclear species was in accordance with the low metal oxide loading and the results from N_2 physisorption measurements. All Mo_xO_y_Fe_xO_y/SBA-15

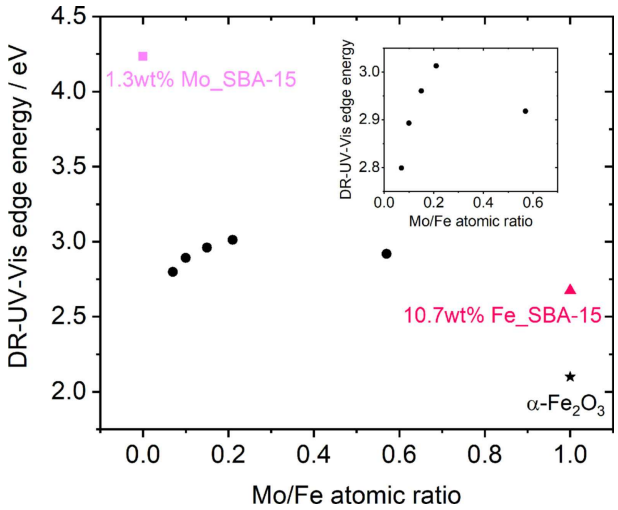

Figure 5. DR-UV-Vis edge energy of Mo_xO_y_Fe_xO_y/SBA-15 samples (dots), 1.3 wt% Mo_SBA-15 (square), 10.7 wt% Fe_SBA-15 (triangle), and α-Fe_2O_3 (star) as function of Mo/Fe atomic ratio. Inset depicts the enlarged trend for the Mo_xO_y_Fe_xO_y/SBA-15 samples.

samples possessed edge energy values higher than those of crystalline α-Fe_2O_3 and 10.7 wt% Fe_SBA-15, corresponding Fe_xO_y/SBA-15 catalyst without molybdenum addition. Accordingly, adding molybdenum induced an increased iron oxide dispersion, and furthermore, a decreased average species size. A dispersion effect of molybdenum on iron oxidic species was also reported for Mo–Fe catalysts supported on activated carbon[29] and Fe–Mo catalysts supported on Al_2O_3.[30] DR-UV-Vis edge energy of the Mo_xO_y_Fe_xO_y/SBA-15 samples increased with increasing Mo/Fe atomic ratio between 0.07/1.0 and 0.21/1.0, indicating a decreasing average species size. Apparently, dispersion effect of molybdenum on Fe_xO_y species was enhanced by increasing Mo/Fe atomic ratio up to 0.21/1.0. A further increased Mo/Fe atomic ratio to 0.57/1.0 yielded a slightly decreased DR-UV-Vis edge energy, indicating a slightly increased average species size. It seemed reasonable that Mo/Fe atomic ratio of 0.57/1.0 induced a slightly increased Mo_xO_y species size due to the increased molybdenum loading. However, Fe_xO_y species remained still smaller and higher dispersed on the support compared to those without molybdenum addition.

2.2. In Situ Characterization

2.2.1. Reducibility of Mo_xO_y_Fe_xO_y/SBA-15 Catalysts

Gaining insight into reducibility of Mo_xO_y_Fe_xO_y/SBA-15 samples was an important starting point for elucidating the influence of adding molybdenum on catalytic performance of Fe_xO_y/SBA-15 catalysts for selective oxidation of propene. Selective oxidation reactions proceed according to the so-called Mars-van-Krevelen mechanism where catalysts are partial reduced and re-oxidized during catalytic cycle.[11,31,32] Suitable selective oxidation catalysts must possess an intermediate metal–oxygen bond strength. A weak metal–oxygen bond strength will lead to mainly total oxidation products. Conversely, if the metal–oxygen bond strength is too strong, catalytic reaction will not proceed.[32]

Figure 6 depicts TPR traces of all Mo_xO_y_Fe_xO_y/SBA-15 samples, 10.7 wt% Fe_SBA-15, and 1.3 wt% Mo_SBA-15. Significant differences in TPR traces were discernible. 10.7 wt% Fe_SBA-15 showed a two-step reduction mechanism where the first and second reduction step were assigned to reduction of Fe^{III} oxidic species to Fe^{II} oxidic species and further reduction to Fe^0, respectively.[25] Adding molybdenum at atomic ratios between 0.07Mo/1.0Fe and 0.21Mo/1.0Fe induced a rising shoulder at the first TPR maxima at higher temperatures while the TPR maxima were shifted to higher temperatures. Conversely, at an atomic ratio of 0.57Mo/1.0Fe, the first TPR maximum was sharp but further shifted to higher temperatures. The shift of the first TPR maxima towards higher temperatures (Figure 7) indicated a lower reducibility of the Fe_xO_y species. Apparently, adding molybdenum induced both an electronic and a dispersion effect on the Fe_xO_y/SBA-15 system. Interactions between Fe^{III} and Mo^{VI} ions during synthesis resulted in higher dispersed and smaller iron oxidic species compared to those without

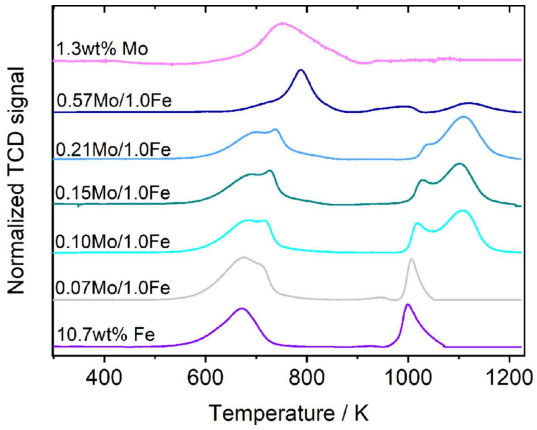

Figure 6. TPR traces of Mo_xO_y_Fe_xO_y/SBA-15 samples at various Mo/Fe atomic ratios, 1.3 wt% Mo_SBA-15, and 10.7 wt% Fe_SBA-15, measured in 5% H_2 in argon at a heating rate of 10 K/min.

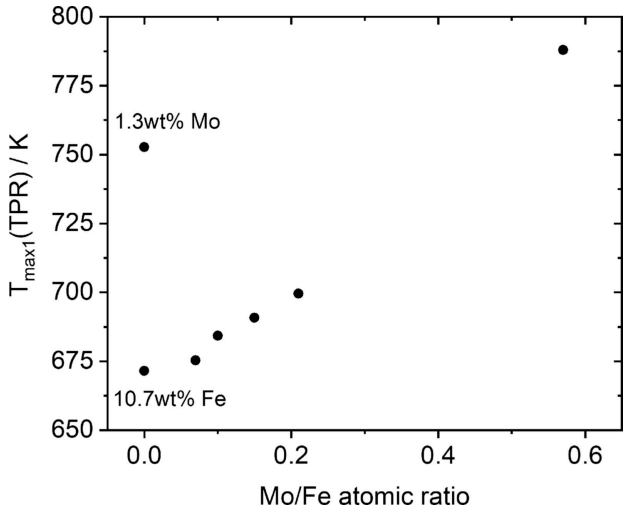

Figure 7. Temperature of the first TPR maxima, $T_{max1}(TPR)$, as function of Mo/Fe atomic ratio. Samples 1.3 wt% Mo_SBA-15 and 10.7 wt% Fe_SBA-15 are depicted at Mo/Fe atomic ratio of 0. TPR experiments were performed in 5% H_2 in argon at a heating rate of 10 K/min.

molybdenum addition. These smaller iron oxidic species with strong interactions to the surface of SBA-15 possessed a lower reducibility. Decreased reducibility with decreased iron oxidic species size was already observed for Fe_xO_y/SBA-15 samples obtained from nitrate precursor.[25] Moreover, adding molybdenum and thereby formed Fe–O–Mo structure units may further inhibit reducibility of the Fe_xO_y system because of a charge transfer between iron and molybdenum species. A postulated electron transfer from iron to oxygen, and further to molybdenum[33] yielded a strengthened Fe–O bond, and thus, hindered the reducibility. The rising shoulder at the first TPR maxima at atomic ratios between 0.07Mo/1.0Fe and 0.21Mo/1.0Fe was assigned to the bimodal particle size distribution of Mo_xO_y_Fe_xO_y/SBA-15 (Figure 3). Smaller Fe^{III} oxidic species resulting from the dispersion effect of molybdenum were correlated with the shoulder at the first TPR maxima at higher temperatures. However, presence of Fe–O–Mo units in small

oligomeric species might also influence the first TPR maxima. Because of an excess of iron compared to molybdenum, reduction of Fe^{III} oxidic species to Fe^{II} oxidic species was still ascribed to the first TPR maxima. Besides bimodal particle size distribution and correlated rising shoulder at the first TPR maxima, the shift of these maxima towards higher temperatures was also induced by the dispersion effect of molybdenum on the Fe_xO_y/SBA-15 system.

The second TPR maxima were also affected by adding molybdenum. Increasing Mo/Fe atomic ratio induced a decreasing intensity and an increasing shift of the second TPR maxima to higher temperatures, while a third TPR maximum arose for atomic ratios up from 0.10Mo/1.0Fe. This new TPR maximum at higher temperatures was attributed to the formation of small, hardly reducible Fe–O–Mo structure units, possibly $Fe_2(MoO_4)_3$-like species. Boulaoued et al.[34] reported for Fe–Mo/KIT-6 strong interactions between iron and molybdenum in mixed oxide catalysts, resulting in a changed reduction mechanism and a more difficult reduction of the iron oxidic species. Interestingly, they ascribed a more important role to molybdenum compared to iron. An analogous influence of adding molybdenum was reported by Kharaji et al.[30] for Fe–Mo/Al_2O_3 catalysts. The authors correlated the new third reduction peak with the presence of hardly reducible Fe–Mo composite oxides, such as $Fe_2(MoO_4)_3$. These findings corroborate the assumed strong interactions between iron and molybdenum, and the involved formation of Fe–O–Mo structure units, in the Mo_xO_y_Fe_xO_y/SBA-15 catalysts.

TPR traces of sample 1.3 wt% Mo_SBA-15 differed significantly from those of Mo_xO_y_Fe_xO_y/SBA-15 catalysts and also from those reported for bulk MoO_3.[34,35] This sample possessed only one single TPR peak. The broad TPR peak was indicative of a high dispersion of small and mainly mononuclear Mo_xO_y species, as observed by XRD and DR-UV-Vis spectroscopy. Furthermore, high reduction temperature of 1.3 wt% Mo_SBA-15 was ascribed to the small Mo_xO_y species possessing strong interactions to the support material.

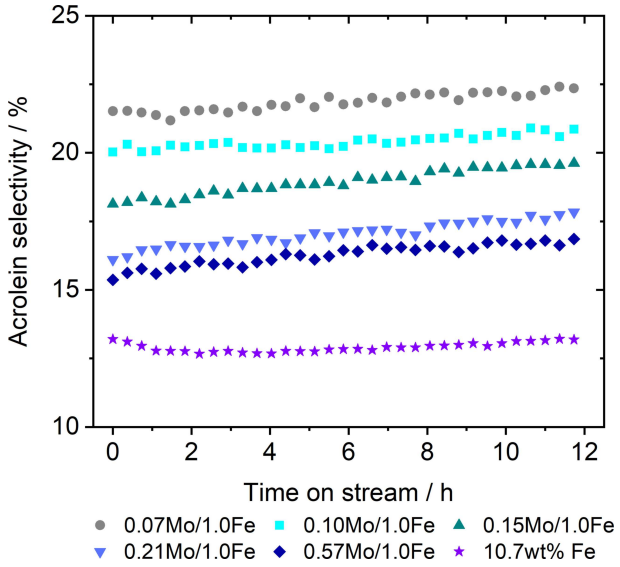

Figure 8. Acrolein selectivity of Mo_xO_y_Fe_xO_y/SBA-15 catalysts at various Mo/Fe atomic ratios and 10.7 wt% Fe_SBA-15 as function of time on stream at 653 K in 5% propene and 5% oxygen in helium.

2.2.2. Catalytic Performance in Selective Oxidation of Propene

Catalytic performance of Mo_xO_y_Fe_xO_y/SBA-15 catalysts in selective oxidation of propene was investigated at 653 K and at comparable propene conversions between 5 and 8%. Figure 8 depicts the evolution of acrolein selectivity as function of time on stream at 653 K for Mo_xO_y_Fe_xO_y/SBA-15 catalysts and 10.7 wt% Fe_SBA-15, respectively. Acrolein selectivity and further product distribution for sample 1.3 wt% Mo_SBA-15 were omitted from the figure. For this low loaded sample, propene conversion was too low to yield reliable results.

Acrolein selectivity showed a significant increase due to adding molybdenum. At an atomic ratio of 0.07Mo/1.0Fe, acrolein selectivity was increased by a factor of 1.7. A further increase in Mo/Fe atomic ratio induced a decrease in acrolein selectivity. However, all Mo_xO_y_Fe_xO_y/SBA-15 catalysts possessed higher acrolein selectivity compared to corresponding Fe_xO_y/SBA-15 catalyst (Figures 8 and 9, left). Besides acrolein as desired selective oxidation product, carbon oxides, CO and CO_2, were the main reaction products in selective oxidation of propene using Mo_xO_y_Fe_xO_y/SBA-15 catalysts. Selectivity towards total oxidation products, CO_x, was significantly decreased after molybdenum addition (Figure 9, right). Lowest acrolein selectivity and highest CO_x selectivity for 10.7 wt% Fe_SBA-15 was in accordance with the largest Fe_xO_y species size and the highest reducibility compared to Mo_xO_y_Fe_xO_y/SBA-15 catalysts. Obviously, Fe–O bond strength without molybdenum addition was weaker leading to a favored total oxidation of propene. The lower reducibility of the Mo_xO_y_Fe_xO_y/SBA-15 catalysts, and the increased Fe–O bond strength, correlated with an increased acrolein selectivity and a lower amount of total oxidation products.

2.3. Correlation Between Molybdenum Induced Effects and Catalytic Performance

As starting point for deducing reliable correlations between adding molybdenum and catalytic performance, Figure 10 depicts acrolein selectivity, DR-UV-Vis edge energy, and temperature of first TPR maxima as function of Mo/Fe atomic ratio. Adding molybdenum induced a dispersion effect on supported iron oxidic species as observed from DR-UV-Vis spectra. This dispersion effect, and furthermore, resulting smaller, higher dispersed Fe_xO_y species could be a possible explanation for the observed catalytic performance of the Mo_xO_y_Fe_xO_y/SBA-15 catalysts. DR-UV-Vis edge energy was used as a measure for particle size of Mo_xO_y_Fe_xO_y/SBA-15 catalysts. The significantly increased DR-UV-Vis edge energy due to adding molybdenum from 2.67 eV for 10.7 wt% Fe_SBA-15 to 2.80 eV for 0.07Mo/1.0Fe_SBA-15 correlated with a significantly increased acrolein selectivity (Figure 10, left). However, the subsequent decrease

in acrolein selectivity with increasing Mo/Fe atomic ratio could not be explained merely based on a dispersion effect. With increasing Mo/Fe atomic ratio, the influence of the electronic effect of molybdenum addition seemed to be crucial for the observed trend in acrolein selectivity. With increasing molybdenum addition, increasing Fe–O bond strength and decreasing reducibility was revealed for Mo_xO_y–Fe_xO_y/SBA-15 catalysts. Decreasing reducibility, expressed as increasing temperature of the first TPR maxima (Figure 10, right), correlated with a decreasing acrolein selectivity. These observations agreed with the postulated intermediate metal–oxygen bond strength being required for selective oxidation catalysts.[32]

2.4. Interpretation of Molybdenum Induced Differences in Structure and Reducibility of Fe_xO_y/SBA-15 Catalysts and their Impact on Catalytic Performance

Figure 11 depicts a schematic representation of the main structural motifs of Mo_xO_y–Fe_xO_y/SBA-15 catalysts dependent on Mo/Fe atomic ratio. Based on this schematic representation, the influence of adding molybdenum on Fe_xO_y/SBA-15 catalysts, i.e. on their structure, reducibility, and catalytic performance, might be interpreted.

Increasing Mo/Fe atomic ratio correlated with a decreasing amount of Fe–O–Fe structure units (Figure 11, (A)). This was ascribed to smaller, higher dispersed Fe_xO_y species of Mo_xO_y–

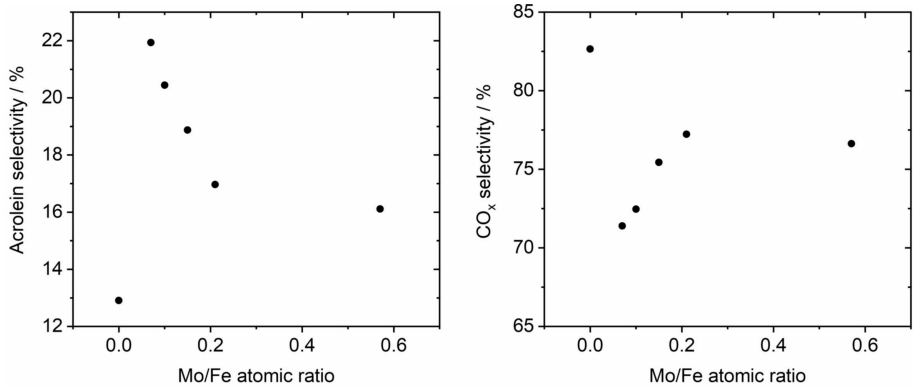

Figure 9. Selectivity towards acrolein (left) and CO_x (right) as function of Mo/Fe atomic ratio. Selectivity was measured at 653 K in 5% propene and 5% oxygen in helium.

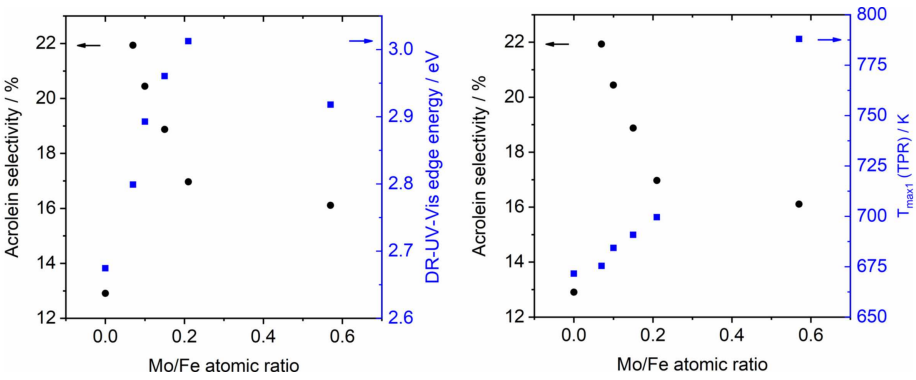

Figure 10. Correlation between acrolein selectivity and DR-UV-Vis edge energy (left) and temperature of first TPR maxima (right) as function of Mo/Fe atomic ratio. Acrolein selectivity was measured at 653 K in 5% propene and 5% oxygen in helium, DR-UV-Vis edge energy was determined at ambient temperature in air, and TPR measurements were conducted in 5% H_2 in argon at 10 K/min up to 1223 K.

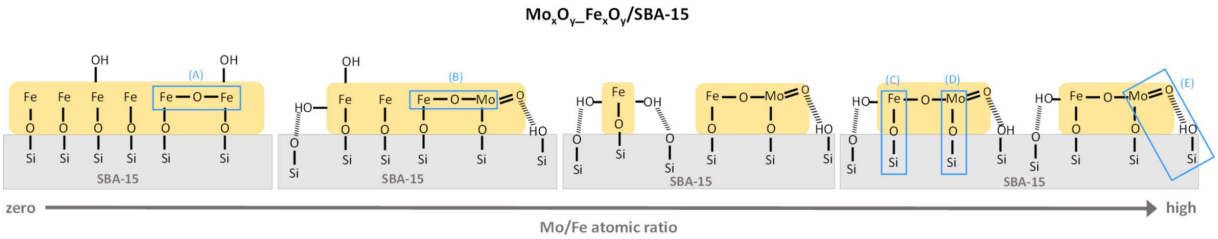

Figure 11. Schematic representation of structural differences of iron oxidic species supported on SBA-15 dependent on Mo/Fe atomic ratio. Only the main structural motifs of Mo_xO_y–Fe_xO_y/SBA-15 catalysts are depicted.

Fe_xO_y/SBA-15 catalysts compared to those of corresponding Fe_xO_y/SBA-15 catalyst without molybdenum. The dispersion effect of molybdenum on Fe_xO_y species induced this decreasing species size. Bridging oxygen atoms in Fe–O–Fe structure units were presumably required for reducibility of Fe_xO_y/SBA-15 catalysts. Accordingly, the decreased Fe_xO_y species size correlated with a decreased reducibility of Mo_xO_y_Fe_xO_y/SBA-15 catalysts compared to corresponding Fe_xO_y/SBA-15 catalyst. Furthermore, with increasing Mo/Fe atomic ratio, Fe–O–Fe structure units were partially replaced by Fe–O–Mo structure units (Figure 11, (B)). Accordingly, the electronic effect of molybdenum on Fe_xO_y species became more important for their reducibility. This electronic effect was associated with an electron transfer from iron to oxygen, and further to molybdenum in Fe–O–Mo structure units. As a result, Fe–O bonds between iron and bridging oxygen atoms were strengthened, yielding a lower reducibility (Figure 11, (B)). Only for highest Mo/Fe atomic ratio, an influence of adding molybdenum on micropore filling was observed. This high Mo/Fe atomic ratio induced a higher degree of micropore filling being ascribed to a higher amount of Fe–O–Si (Figure 11, (C)) and Mo–O–Si bonds (Figure 11, (D)), as well as hydrogen bonds (Figure 11, (E)). These hardly reducible Fe–O–Si and Mo–O–Si bonds additionally hindered the reducibility of Mo_xO_y_Fe_xO_y/SBA-15 catalysts. Therefore, selectivity towards acrolein decreased with increasing Mo/Fe atomic ratio. Highest acrolein selectivity for an atomic ratio of 0.07Mo/1.0Fe might be explained by an optimal combination of intermediate reducibility and high electron transfer efficiency in Fe_xO_y oligomers. This might facilitate the formation of nucleophilic surface oxygen species, yielding a higher acrolein selectivity. Despite decreasing reducibility with increasing Mo/Fe atomic ratio, formation of nucleophilic oxygen species might still be favored in Mo_xO_y_Fe_xO_y/SBA-15 catalysts. This might explain the higher acrolein selectivity of all Mo_xO_y_Fe_xO_y/SBA-15 catalysts compared to that of corresponding Fe_xO_y/SBA-15 catalyst. However, acrolein selectivity as function of Mo/Fe atomic ratio was presumably determined by a combination of various effects, such as reducibility, species size, and electron transfer efficiency. Characterization of Mo_xO_y_Fe_xO_y/SBA-15 catalysts corroborated the assumed importance of Fe–O–Fe structure units (Figure 11, (A)) in selective oxidation of propene.

3. Conclusion

The synthesis of iron and molybdenum mixed oxides on mesoporous SBA-15 yielded suitable binary model catalysts for investigating structure-activity correlations. Invariant iron loading permitted investigating the influence of adding molybdenum on Fe_xO_y/SBA-15 catalysts. Mo_xO_y and Fe_xO_y species of the Mo_xO_y_Fe_xO_y/SBA-15 catalysts were highly dispersed on SBA-15 without changing the structure of the support. Formation of long-range ordered structures was excluded. Adding molybdenum yielded a pronounced dispersion effect on supported iron oxidic species. Accordingly, average species size was decreased compared to Fe_xO_y/SBA-15 catalyst. Increasing atomic ratio up to 0.21Mo/1.0Fe was accompanied by decreasing species sizes. Strong interactions between iron and molybdenum during synthesis resulted in formation of Fe–O–Mo structure units. At higher Mo/Fe atomic ratio, these strong interactions probably induced small $Fe_2(MoO_4)_3$-like species. Moreover, adding molybdenum significantly influenced the reducibility of Fe_xO_y/SBA-15. Lower reducibility due to adding molybdenum was ascribed to both dispersion and electronic effect of molybdenum. Smaller and higher dispersed iron oxidic species possessed a lower reducibility compared to larger and less dispersed species. Additionally, a charge transfer from iron to oxygen, and further to molybdenum in Fe–O–Mo structure units yielded a strengthened Fe–O bond and, hence, hindered reducibility. The change of the two-step reduction mechanism for 10.7 wt% Fe_SBA-15 towards a three-step reduction mechanism for Mo_xO_y_Fe_xO_y/SBA-15 catalysts corroborated the presence of small, hardly reducible Fe–O–Mo structure units.

Catalytic performance of Mo_xO_y_Fe_xO_y/SBA-15 was studied under selective propene oxidation conditions. Adding molybdenum resulted in an increased acrolein selectivity and a decreased selectivity towards total oxidation products. Increasing Mo/Fe atomic ratio induced a decreasing acrolein selectivity while still being higher than that of Fe_xO_y/SBA-15 catalyst. Influence of adding molybdenum on catalytic performance was correlated with both dispersion and electronic effect of molybdenum. The strengthened Fe–O bonds, and the lower reducibility, with increasing Mo/Fe atomic ratio, led to an inferior total oxidation. This coincided with an intermediate Fe–O bond strength being required for selective oxidation of propene.

Experimental Section

Sample Preparation

Mesoporous silica SBA-15 was prepared according to Zhao et al..[14,36] Mixed iron and molybdenum oxide catalysts supported on SBA-15 were prepared by incipient wetness technique and denoted Mo_xO_y_Fe_xO_y/SBA-15. Therefore, an aqueous solution of ammonium iron(III) citrate (~18% Fe, Roth) and ammonium heptamolybdate tetrahydrate (≥99%, Fluka) was used. The pH value of the aqueous oxide precursor solution was adjusted to 7.5–8. After drying in air for 24 h, calcination was carried out at 723 K for 5 h. To investigate the influence of adding molybdenum on Fe_xO_y/SBA-15 catalysts, iron loading was kept invariant, while Mo/Fe atomic ratio was varied between 0.07/1.0 and 0.57/1.0. According to the Mo/Fe atomic ratio, samples were denoted 0.07Mo/1.0Fe/SBA-15, 0.10Mo/1.0Fe/SBA-15, 0.15Mo/1.0Fe/SBA-15, 0.21Mo/1.0Fe/SBA-15, and 0.57Mo/1.0Fe/SBA-15. Furthermore, samples with 1.3 wt% Mo supported on SBA-15, 1.3 wt% Mo_SBA-15, and with 10.7 wt% Fe supported on SBA-15, 10.7 wt% Fe_SBA-15, were prepared as references. Metal oxide loadings of the samples were quantified by X-ray fluorescence spectroscopy. Moreover, CHN analysis was performed to confirm a complete decomposition of the precursors.

Sample Characterization

X-Ray Fluorescence Analysis

Quantitative analysis of the metal oxide loadings on SBA-15 was conducted by X-ray fluorescence spectroscopy on an AXIOS X-ray spectrometer (2.4 kW model, PANalytical), equipped with a Rh K_α X-ray source, a gas flow detector, and a scintillation detector. Prior to measurements, samples were mixed with wax (Hoechst, Merck), ratio 1:1, and pressed into pellets of 13 mm diameter. Quantification was performed by standardless analysis using the software package SuperQ5 (PANalytical).

Elemental Analysis

Elemental contents of C, H, and N were determined using a Thermo FlashEA 1112 Organic Elemental Analyzer (ThermoFisher Scientific) with CHNS–O configuration.

Powder X-Ray Diffraction

Powder X-ray diffraction patterns were obtained using an X'Pert PRO diffractometer (PANalytical, 40 kV, 40 mA) in theta/theta geometry equipped with a solid-state multi-channel detector (PIXel). Cu K_α radiation was used. Wide-angle diffraction scans were conducted in reflection mode. Small-angle diffraction patterns were measured in transmission mode from 0.4° through 6° 2θ in steps of 0.013° 2θ with a sampling time of 90 s/step.

Nitrogen Physisorption

Nitrogen adsorption/desorption isotherms were measured at 77 K using a BELSORP Mini II (BEL Inc. Japan). Prior to measurements, the samples were pre-treated under reduced pressure (10^{-2} kPa) at 368 K for 35 min and kept under the same pressure at 448 K for 15 h (BELPREP II vac).

DR-UV-Vis Spectroscopy

Diffuse reflectance UV-Vis (DR-UV-Vis) spectroscopy was conducted on a two-beam spectrometer (V-670, Jasco) using a barium sulfate coated integration sphere. (Scan speed 100 nm/min, slit width 5.0 nm (UV-Vis) and 20.0 nm (NIR), and spectral region 220–2000 nm). SBA-15 was used as white standard for all samples.

Temperature-Programmed Reduction

Temperature-programmed reduction (TPR) was performed using a BELCAT_B (BEL Inc. Japan). Samples were placed on silica wool in a silica glass tube reactor. Evolving water was trapped using a molecular sieve (4 Å). Gas mixture consisted of 5% H_2 in 95% Ar with a total gas flow of 40 ml/min. Heating rate used was 10 K/min to 1223 K. A constant initial sample weight of 0.03 g was used and H_2 consumption was continuously monitored by a thermal conductivity detector.

Catalytic Measurements

Quantification of catalytic activity in selective oxidation of propene was performed using a laboratory fixed-bed reactor connected to an online gas chromatography system (CP-3800, Varian) and a mass spectrometer (Omnistar, Pfeiffer Vacuum). The fixed-bed reactor consisted of a SiO_2 tube (30 cm length, 9 mm inner diameter) placed vertically in a tube furnace. A P3 frit was centered in the SiO_2 tube in the isothermal zone, where the sample was placed. The samples were diluted with boron nitride (99.5%, Alfa Aesar) to achieve a constant volume in the reactor and to minimize thermal effects. Overall sample masses were 0.25 g. The reactor was operated at low propene conversion levels (5–8%) to ensure differential reaction conditions. For catalytic testing in selective oxidation of propene, a gas mixture of 5% propene and 5% oxygen in helium was used in a temperature range of 298–653 K with a heating rate of 5 K/min. Reactant gas flow rates of propene, oxygen, and helium were adjusted through separate mass flow controllers (Bronkhorst) to a total flow of 40 ml/min. All gas lines and valves were preheated to 473 K. Hydrocarbons and oxygenated reaction products were analyzed using a Carbowax 52CB capillary column, connected to an Al_2O_3/MAPD capillary column (25 m × 0.32 mm) or a fused silica restriction (25 m × 0.32 mm), each connected to a flame ionization detector (FID). Permanent gases (CO, CO_2, N_2, O_2) were separated and analyzed using a "Permanent Gas Analyzer" (CP-3800, Varian) with a Hayesep Q (2 m × 1/8″) and a Hayesep T packed column (0.5 m × 1/8″) as precolumns combined with a back flush. For separation, a Hayesep Q packed column (0.5 m × 1/8″) was connected via a molecular sieve (1.5 m × 1/8″) to a thermal conductivity detector (TCD). Additionally, product and reactant gas flow were continuously monitored by a connected mass spectrometer (Omnistar, Pfeiffer) in a multiple ion detection mode.

Acknowledgements

The authors are grateful to A. Knoch and S. Schwarz for assistance during synthesis and N_2 physisorption measurements, respectively. J. Krone is acknowledged for CHN elemental analysis.

Conflict of Interest

The authors declare no conflict of interest.

Keywords: dispersion effect · electronic effect · green chemistry · heterogeneous catalysis · iron oxides

[1] N. R. Shiju, V. V. Guliants, *Appl. Catal. A* **2009**, *356*, 1–17.
[2] L. Liu, X. P. Ye, J. J. Bozell, *ChemSusChem* **2012**, *5*, 1162–1180.
[3] B. Katryniok, S. Paul, V. Bellière-Baca, P. Rey, F. Dumeignil, *Green Chem.* **2010**, *12*, 2079–2098.
[4] P. Anastas, N. Eghbali, *Chem. Soc. Rev.* **2010**, *39*, 301–312.
[5] "The Propylene Gap: How Can It Be Filled? – American Chemical Society", can be found under https://www.acs.org/content/acs/en/pressroom/cutting-edge-chemistry/the-propylene-gap-how-can-it-be-filled.html, **2018**.
[6] a) R. K. Grasselli, *Catal. Today* **1999**, *49*, 141–153; b) B. L. Kniep, T. Ressler, A. Rabis, F. Girgsdies, M. Baenitz, F. Steglich, R. Schlögl, *Angew. Chem. Int. Ed. Engl.* **2004**, *43*, 112–115.
[7] U. S. Ozkan, R. B. Watson, *Catal. Today* **2005**, *100*, 101–114.
[8] A. F. Holleman, E. Wiberg, N. Wiberg, *Lehrbuch der anorganischen Chemie*, de Gruyter, Berlin, New York, **2007**.
[9] a) S. Enthaler, K. Junge, M. Beller, *Angew. Chem. Int. Ed. Engl.* **2008**, *47*, 3317–3321; b) A. S. Al-Fatesh, A. H. Fakeeha, A. A. Ibrahim, W. U. Khan, H. Atia, R. Eckelt, B. Chowdhury, *J. Chin. Chem. Soc.* **2016**, *63*, 205–212.
[10] J. C. Védrine, G. Coudurier, J.-M. M. Millet, *Catal. Today* **1997**, *33*, 3–13.
[11] B. Grzybowska-Świerkosz, *Top. Catal.* **2000**, *11–12*, 23–42.
[12] a) M. M. Lin, *Appl. Catal. A* **2001**, *207*, 1–16; b) C. Zhao, I. Wachs, *J. Catal.* **2008**, *257*, 181–189.

[13] J. He, Y. Li, D. An, Q. Zhang, Y. Wang, *J. Nat. Gas Chem.* **2009**, *18*, 288–294.
[14] D. Zhao, *Science* **1998**, *279*, 548–552.
[15] a) M. Kruk, M. Jaroniec, C. H. Ko, R. Ryoo, *Chem. Mater.* **2000**, *12*, 1961–1968; b) C.-M. Yang, B. Zibrowius, W. Schmidt, F. Schüth, *Chem. Mater.* **2004**, *16*, 2918–2925.
[16] K. S. W. Sing, *Pure Appl. Chem.* **1985**, *57*, 603–619.
[17] A. Ungureanu, B. Dragoi, A. Chirieac, S. Royer, D. Duprez, E. Dumitriu, *J. Mater. Chem.* **2011**, *21*, 12529.
[18] J. R. A. Sietsma, J. D. Meeldijk, M. Versluijs-Helder, A. Broersma, A. J. van Dillen, P. E. d. Jongh, K. P. d. Jong, *Chem. Mater.* **2008**, *20*, 2921–2931.
[19] R. Huirache-Acuña, B. Pawelec, E. Rivera-Muñoz, R. Nava, J. Espino, J. L. G. Fierro, *Appl. Catal. B* **2009**, *92*, 168–184.
[20] S. Brunauer, P. H. Emmett, E. Teller, *J. Am. Chem. Soc.* **1938**, *60*, 309–319.
[21] E. P. Barrett, L. G. Joyner, P. P. Halenda, *J. Am. Chem. Soc.* **1951**, *73*, 373–380.
[22] M. A. Smith, R. F. Lobo, *Microporous Mesoporous Mater.* **2010**, *131*, 204–209.
[23] G. Koch, L. Schmack, T. Ressler, *ChemistrySelect* **2016**, *1*, 2040–2049.
[24] P. Pfeifer, *Phys. Rev. Lett.* **1989**, *62*, 1997–2000.
[25] N. S. Genz, D. Baabe, T. Ressler, *J. Anal. Methods Chem.* **2017**, *2017*, 1–13.
[26] T. Abe, Y. Tachibana, T. Uematsu, M. Iwamoto, *J. Chem. Soc., Chem. Commun.* **1995**, 1617–1618.
[27] R. S. Weber, *J. Catal.* **1995**, *151*, 470–474.
[28] Y. Lou, H. Wang, Q. Zhang, Y. Wang, *J. Catal.* **2007**, *247*, 245–255.
[29] W. Ma, E. L. Kugler, J. Wright, D. B. Dadyburjor, *Energy Fuels* **2006**, *20*, 2299–2307.
[30] A. G. Kharaji, A. Shariati, M. A. Takassi, *Chin. J. Chem. Eng.* **2013**, *21*, 1007–1014.
[31] G. Centi, F. Cavani, F. Trifirò, *Selective oxidation by heterogeneous catalysis*, Kluwer Acad./Plenum Publ, New York, **2001**.
[32] R. Grasselli, *Top. Catal.* **2002**, *21*, 79–88.
[33] S. Qin, C. Zhang, J. Xu, Y. Yang, H. Xiang, Y. Li, *Appl. Catal. A* **2011**, *392*, 118–126.
[34] A. Boulaoued, I. Fechete, B. Donnio, M. Bernard, P. Turek, F. Garin, *Microporous Mesoporous Mater.* **2012**, *155*, 131–142.
[35] H. Zhang, J. Shen, X. Ge, *J. Solid State Chem.* **1995**, *117*, 127–135.
[36] D. Zhao, Q. Huo, J. Feng, B. F. Chmelka, G. D. Stucky, *J. Am. Chem. Soc.* **1998**, *120*, 6024–6036.

Manuscript received: June 26, 2019
Revised manuscript received: July 13, 2019

